Systematic simulation studies on the penetration of resonant magnetic perturbations in EAST

H. W. Zhang, X. Lin, Z. W. Ma*, W. Zhang, T. E. Bagwell

Institute for Fusion Theory and Simulation, Department of Physics, Zhejiang University, Hangzhou 310027, China

Abstract: The penetration properties of the n = 1 resonant magnetic perturbations (RMPs) with toroidal rotation are systematically studied by the upgraded three-dimensional toroidal magnetohydrodynamic code CLTx. Through both linear and nonlinear simulations, it is found that in the presence of toroidal plasma rotation, the saturation state for high resonant harmonics is obtained in linear simulations due to the mode becoming unlocked from the internal magnetic islands. While in nonlinear simulations, nonlinear effects become important when the toroidal plasma rotation is not included. The zonal component resulted from the nonlinear mode coupling is necessary for the saturation of the whole system including the internal kink mode and the m/n = 2/1 tearing mode. The simulations on RMP penetration demonstrate that the mode coupling is associated with the toroidal effect rather than a consequence of nonlinear effects. With a low resistivity, the single-harmonic-RMP is hard to penetrate the mode-rational surface because of the plasma screening effect, resulting in a truncation on the radial mode structure. On the other hand, the non-resonant components in the multiple-harmonic-RMP could largely reduce the effect of the plasma shielding and result in that the RMP is able to penetrate deeply into the central plasma region through the poloidal harmonics coupling.

Keywords: resonant magnetic perturbation, penetration, nonlinear effects, toroidal effect

* Email address: zwma@zju.edu.cn

1 Introduction

Resonant magnetic perturbation (RMP) is very efficient for controlling the edge localized mode (ELM) [1] in H-mode [2] discharge in Tokamaks. However, MHD (magnetohydrodynamic) theoretical analysis [3, 4], numerical simulations [5-18], and plasma experiments [19-21] have demonstrated that RMP penetration theory based on the vacuum model is inaccurate or even completely invalid. Meanwhile, RMP penetration is especially sensitive to plasma response in the presence of dynamical effects, like plasma rotation [11, 22], two-fluid effects [9, 12, 23, 24], screen current [25, 26], nonlinear mode coupling [6, 9, 17, 27], etc.

Linearized models in analytical and numerical studies of the influence of plasma response on RMP penetration have been widely adopted and have shown high efficiency in calculation speed and great feasibility compared with plasma experimental results. Results obtained by the MARS-F code based on a linearized single-fluid MHD model have successfully explained the offset of the optimal coil phase in edge localized mode (ELM) control experiments with the n = 1 and 2 RMPs in EAST (Experimental Advanced Superconducting Tokamak) [10, 28] and the n = 2 RMP in the ASDEX Upgrade (Axially Symmetric Divertor Experiment) [28, 29], where n represents the toroidal mode number. The simulation results from the M3D-C^1 code adopting a linearized two-fluid model have demonstrated that the penetrated RMP field reaches its maximum value when the perpendicular electron rotation vanishes at the mode-rational surface [12, 24]. However, nonlinear simulations of RMPs have indicated that nonlinear effects are crucial and exhibit some dynamical features that are not present in purely linear simulations, such as the density pumpout due to the n = 0 component coupled with n = 2 perturbations [6] and the generation of high-order magnetic islands from the coupling of different harmonics [9]. In addition, the resonant amplification of RMPs due to the coupling between the non-resonant kink component ($|m| > |nq|$, where m is the poloidal mode number, and q is the safety factor) and the resonant m component has been observed in both linear and nonlinear modelings, respectively, by the MARS-F code [30] and the JOREK code [6], The validity criterion for the linear model can be written simply as the overlap condition $|\partial\zeta_r / \partial r| < 1$ (where ζ_r is the plasma displacement normal to the equilibrium magnetic field) after considering plasma response [27, 28]. Although the linear model has the advantages of being numerically and analytically efficient while still maintaining great validity in RMP calculations, nonlinear mode couplings, however, should not be ignored in some cases [27, 28].

In our previous work [18], the code CLT was upgraded to CLTx for studying RMP penetration in EAST based on the linear and nonlinear resistive MHD equations. Results from linear simulations of RMPs applied to studies regarding ELM mitigation discharge 52340 in EAST have agreed well with those obtained from the MARS-F code. However, subsequent numerical simulation studies with different adopted resistivities suggest that the amplitude reduction and the phase shift of the resonant harmonics due to plasma response increase with decreasing resistivity. In this work, the nonlinear terms are retained in the CLTx code for studying the nonlinear effects on RMP penetration. The influences of toroidal rotation, nonlinear mode coupling, and toroidal effect on RMP penetration will be analyzed and discussed. The outline of the present paper is as follows: Section 2 introduces the simulation model used in the CLTx code; Section 3 presents the results of the linear and nonlinear simulations for RMP penetration and the influences of toroidal rotation; Section 4 gives the toroidal effect on RMP penetration in detail; and finally, the results of the present paper are summarized in Section 5.

2 Simulation model for CLTx

In the CLTx code, we adopted the full set of single fluid, resistive MHD equations including dissipations [18, 31], i.e.,

$$\partial_t \rho = -\nabla \cdot (\rho \mathbf{v}) + \nabla \cdot \left[D\nabla(\rho - \rho_0) \right], \tag{1}$$

$$\partial_t p = -\mathbf{v} \cdot \nabla p - \Gamma p \nabla \cdot \mathbf{v} + \nabla \cdot \left[\kappa \nabla (p - p_0) \right], \tag{2}$$

$$\partial_t \mathbf{v} = -\mathbf{v} \cdot \nabla \mathbf{v} + (\mathbf{J} \times \mathbf{B} - \nabla p) / \rho + \nabla \cdot \left[\nu \nabla (\mathbf{v} - \mathbf{v_0}) \right], \tag{3}$$

$$\partial_t \mathbf{B} = -\nabla \times \mathbf{E}, \tag{4}$$

with

$$\mathbf{E} = -\mathbf{v} \times \mathbf{B} + \eta (\mathbf{J} - \mathbf{J_0}), \tag{5}$$

$$\mathbf{J} = \nabla \times \mathbf{B}, \tag{6}$$

where ρ, p, $\mathbf{v}$, $\mathbf{B}$, $\mathbf{E}$, and $\mathbf{J}$ are the plasma density, thermal pressure, plasma velocity, magnetic field, electric field, and current density, respectively. The subscript ‘0’ denotes equilibrium quantities. Γ (= 5/3) is the ratio of specific heat of the plasma. The variables are normalized as: $\mathbf{B}/B_{00} \to \mathbf{B}$, $\mathbf{x}/a \to \mathbf{x}$, $\rho/\rho_{00} \to \rho$, $\mathbf{v}/v_A \to \mathbf{v}$, $t/\tau_A \to t$, $p/\left(B_{00}^2/\mu_0\right) \to p$, $\mathbf{J}/(B_{00}/\mu_0 a) \to \mathbf{J}$, $\mathbf{E}/(v_A B_{00}) \to \mathbf{E}$, and $\eta/\left(\mu_0 a^2/\tau_A\right) \to \eta$, where a is equal to one meter, $v_A = B_{00}/\sqrt{\mu_0 \rho_{00}}$ is the Alfvén speed, and $\tau_A = a/v_A$ is the Alfvén time. B_{00} and ρ_{00} are the initial magnetic field and plasma density at the magnetic axis, respectively. Note that the Hall term [32] in the generalized Ohm’s law is not included, thus diamagnetic drifts due to two-fluid effects are not present in the current model.

The simulation domain constructed in the CLTx code has been extended beyond the last closed magnetic surface to the scrape-off layer (SOL) with the inclusion of the X-point. The normalized parameters used in all simulations herein are fixed to be $D=1\times10^{-6}$, $\kappa=5\times10^{-5}$, and $\mu=1\times10^{-6}$. The spatial distribution of the time-independent resistivity is determined by the initial normalized plasma temperature T with $\eta=\eta_0\cdot T^{-3/2}$, where η_0 is the resistivity at the magnetic axis and corresponds to a resistivity minimum since the temperature is maximum at this axis. A mesh consisting of $256\times16\times256$ points in (R, ϕ, Z) is utilized for all simulations. In the CLTx code, the basic straight field line coordinates $(\sqrt{\psi_n}, \theta_s, \phi)$ [18, 33] are used for spectrum analysis, where $\sqrt{\psi_n}$ is the square root of the normalized poloidal flux ψ_n , θ_s is the generalized poloidal angle, and ϕ is the toroidal angle.

The initial equilibria are reconstructed from EAST discharge 52340 at 3150 ms [10] and discharge 62585 at 3800 ms [34] by EFIT (Equilibrium Fitting code) [35]. The safety factor q profiles for each discharge and the toroidal rotation ω_t profile of discharge 52340 are given in Figure 1.

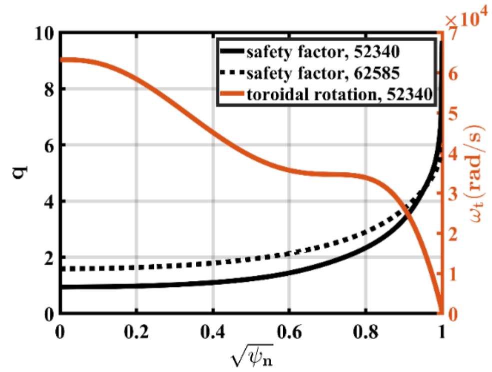

Figure 1. Initial profiles of the safety factor q for EAST discharge 52340 at 3150 ms and 62585 at 3800 ms, and the toroidal rotation ω_t for EAST discharge 52340 at 3150 ms.

3 Linear and nonlinear saturations with the presence of RMP

In our previous linear benchmark study for the equilibrium of discharge 52340, the magnetic island at high rational surfaces ($q > 1$) reaches a level of significant saturation, however the inner unstable $m/n = 1/1$ kink mode is still in the linear growth stage [18]. To understand the detailed saturation mechanisms of magnetic islands in linear simulations, comparisons between linear and nonlinear simulations with a relatively large resistivity $\eta_0=5\times10^{-7}$ are performed in the present paper. The RMP coils set up in the CLTx code is I_{coil} = 10 kAt (kilo-Amp-turns), n = 1, $\Delta\Phi=0$, where $\Delta\Phi$ is the relative phase difference between the upper and lower coils [28]. The role of the plasma toroidal rotation on mode saturation is also studied in the present paper by artificially including plasma rotation, however, the artificial toroidal rotation speed is constrained to be sub-sonic. Under these conditions, the resultant inertial force on the equilibria due to toroidal rotation is less than one percent of the entire pressure gradient force and is not included in the governing equations of the CLTx code initially. The same considerations are taken for discharges 52340 and 62558 discussed below.

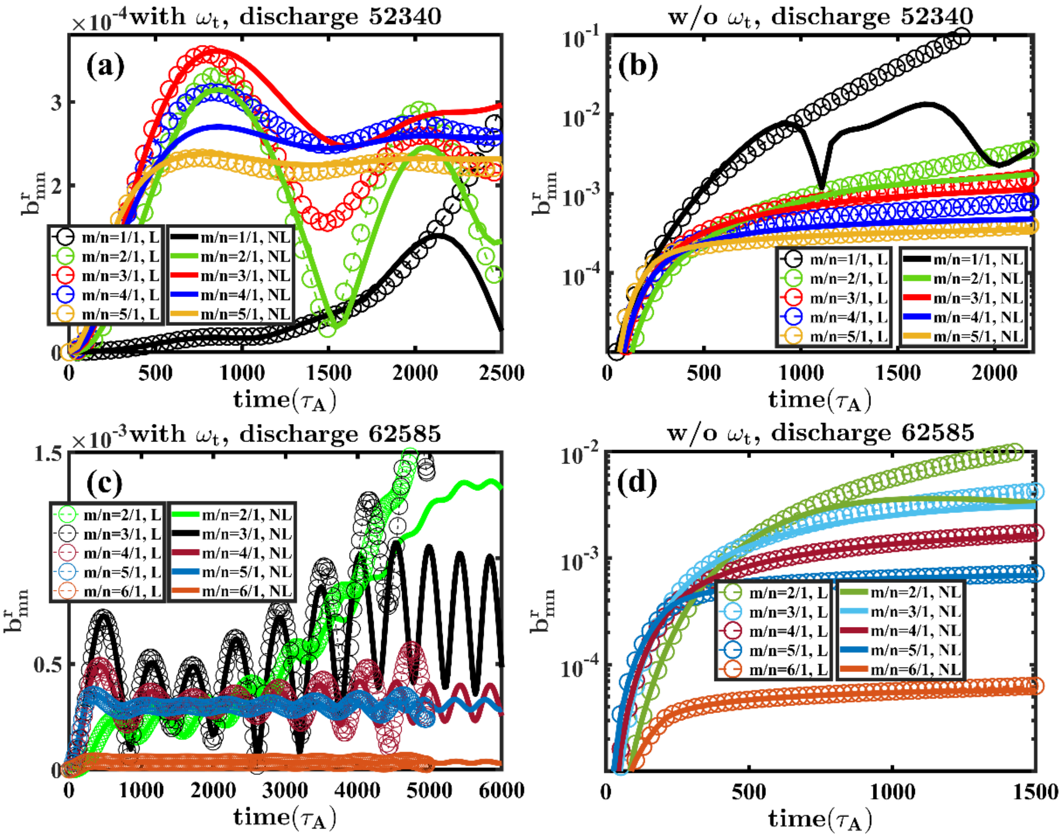

Figure 2. Time evolutions of resonant harmonics $b^r_{m/n}$ at different rational surfaces with both linear (dashed lines with circles, indicated by 'L', the same below) and nonlinear (solid lines, indicated by 'NL', the same below) simulations for discharge 52340 (a) with toroidal rotation (the $m/n = 1/1$ harmonics are artificially reduced by multiplying a factor of 0.02) and (b) without toroidal rotation, as well as for discharge 62585 (c) with toroidal rotation (the $m/n = 2/1$ harmonics are artificially reduced by multiplying a factor of 0.25) and (d) without toroidal rotation. The vertical axes of the left-hand side panels are scaled linearly, while the vertical axes of the right-hand side panels are scaled logarithmically.

Time evolutions of resonant harmonics $b^r_{m,n}$ driven by RMP for the equilibrium of discharge 52340 with the toroidal rotation are shown in Figure 2 (a). Nonlinear effects in the pedestal region ($m \geq 5$, $n = 1$) are ignorable but the chosen resistivity $\eta_0 = 5\times10^{-7}$ is artificially enlarged by two orders of magnitude compared with the experimental parameter. Evidently, the only significant difference between the linear and nonlinear simulations is that the unstable m/n = 1/1 kink mode becomes saturated due to nonlinear mode coupling after 2100 τ_A. These results suggest that nonlinear effects are not important before the internal kink instability begins to play a role in the overall plasma dynamics, although it should be noted that the islands overlap condition $|\partial\zeta_r / \partial r| < 1$ [27, 28] is not satisfied in the pedestal after taking the plasma response into account [18].

Figure 2 (b) shows the simulation results for discharge 52340 without the toroidal rotation. No saturation for any harmonic is observed in the linear result without toroidal rotation. While in the nonlinear case, the m/n = 1/1 kink mode becomes saturated as expected due to nonlinear mode coupling, which also contributes to the reduction of higher harmonics ($m \geq 2$, $n = 1$).

The second set of simulations with EFIT reconstructed equilibrium for EAST discharge 62585 at 3800 ms [34] is carried out both with and without the toroidal rotation. All parameters and the RMP configurations are the same as those in the preceding simulations. The safety factor profile of discharge 62585 is monotonous with q_{min} = 1.59 and q_{95} = 4.87 as shown in Figure 1. The toroidal rotation profile of discharge 52340 in Figure 1 is artificially added in the static equilibrium of discharge 62585 due to the lack of a self-consistent rotation profile. The results of discharge 62585 in Figure 2 (c) and (d) show similar tendencies in comparison with those of discharge 52340. All resonant harmonics with high poloidal mode number ($m \geq 3$, $n = 1$) become saturated both with and without toroidal rotation in both the linear and nonlinear simulations. Uniquely, the lowest resonant m/n = 2/1 tearing mode exhibits a continuous growth (the oscillation of the m/n = 2/1 tearing mode is due to the mode rotating with the toroidal flow) in its linear simulation, while in the nonlinear simulation this particular mode becomes saturated due to the generation of the n = 0 zonal component through nonlinear mode coupling [36, 37].

Similar saturated time-independent solutions for stable equilibria were reported in the linearized MHD simulations carried out with the M3D-C^1 code [24]. However, in our simulations of unstable equilibria with the toroidal rotation, the linearly saturated solutions for the n = 1 RMP are obtained for the harmonics with $m \geq 2$ in discharge 52340 and $m \geq 3$ in discharge 62585 with the presence of toroidal rotation. The same saturated results for high harmonics obtained in both linear and nonlinear simulations with the toroidal rotation further demonstrate the validity of the linear model used in the previous researches of the MARS-F and CLTx code [10, 18].

With different amplitudes of RMP I_{coil} = 5kAt, 10kAt, and 20kAt, the time evolutions of the m/n = 4/1 harmonic at the q = 4 rational surface for EAST discharge 52340 with the toroidal rotation are given in Figure 3. The shielding effects due to plasma response are almost identical for all cases with the shielding ratio ($b^r_{response} / b^r_{vacuum}$) approaching approximately 60%. Meanwhile, the overall qualitative evolutions among all cases are almost identical, that is, the modes for all cases become saturated after 3000 τ_A . The saturation amplitude of the high resonant harmonic with plasma response is linearly proportional to the intensity of the vacuum RMP. Also, the increase of the RMP intensity does not lead to breakdown of high resonant harmonics.

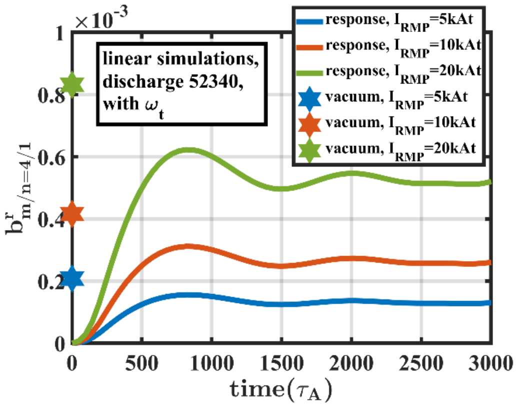

Figure 3. Time evolutions of resonant harmonics $b^r_{m/n}$ at the q = 4 rational surface for EAST discharge 52340 with toroidal rotation. The amplitude of the RMP is adjusted by 5 kAt (blue), 10 kAt (red), and 20 kAt (green). The hexagrams along the vertical axis mark out the amplitudes of the resonant m/n = 4/1 harmonic in vacuum for each case.

4 Toroidal effect on the penetration of RMP

In this section, we mainly focus on toroidal coupling effect on penetration of RMP in the interior resonant surfaces. Thus, the SOL region is not included in this study. In order to reduce the impact of boundary treatment, the safety factor for discharge 52340 is truncated to a finite value at the plasma boundary and the q = 6 rational surface is slightly shifted inward. The reconstructed equilibrium from the QSOLVER code [38] is shown by the red line of Figure 7. The RMP field is applied inside the plasma boundary where the generalized poloidal angle θ_s can be defined accurately. Usually, RMP fields generated by realistic coils contain multiple resonant and non-resonant harmonics and the penetration of a specific harmonic could be influenced by others [6, 30]. In this section, instead of the RMP fields directly calculated from the realistic coils, we chose the RMP to be artificially composited with different harmonics of the perturbed magnetic flux $\delta\psi_{\mathbf{RMP}}$ as follows,

$$\delta\psi_{\mathbf{RMP}} = \sum_{m,n} \delta\psi_{m,n} \cos\left(m\theta_s(\psi_n) + n\phi\right)\left(1 + \tanh\left(\left(\psi_n - \psi_0\right) / d_{RMP}\right)\right) / m \,, \tag{7}$$

where $\delta\psi_{m,n}$ is on the order of 10^{-5}, corresponding to currents of several kiloamperes (kA), ψ_n is the normalized poloidal flux, $\psi_0 = 0.90$, and $d_{RMP} = 0.02$.

With varying combinations of different RMP harmonics, the response of the radial perturbation of the resonant magnetic field $b^r_{m/n=2/1}$ at the q = 2 rational surface is investigated. The reason for choosing the q = 2 surface is that the penetration mechanisms for different harmonics should be qualitatively consistent and the spectrum analysis is more accurate for lower harmonics. In the first subsection below, we discuss the simulation results of the single-harmonic-RMP and the double-harmonic-RMP, in which the different roles played by resonant and non-resonant components will be illustrated. In the second subsection, the poloidal harmonics filtering analysis and the multiple-harmonic-RMP simulation results are presented to confirm the importance of poloidal harmonics coupling on RMP penetration.

4.1 The single-harmonic-RMP and the double-harmonic-RMP

In this subsection, the single-harmonic-RMP is chosen to be two different amplitudes with $\delta\psi_{2,1} = 2\times10^{-5}$ and $\delta\psi_{2,1}(\times2) = 4\times10^{-5}$ while the double-harmonic-RMP consists of the *m/n* = 2/1 harmonic and another higher *m* harmonic (*m* > 2, *n* = 1) with the same amplitude $\delta\psi_{m,n} = 2\times10^{-5}$. A large resistivity ($\eta_0 = 10^{-6}$) is used and all simulations are carried out based on the fully nonlinear simulation code CLT. Figure 4 shows time evolutions for $b^r_{m/n=2/1}$ with two different harmonic compositions of RMP. It is evident that, compared with the single *m/n* = 2/1 harmonic RMP with $\delta\psi_{2,1} = 2\times10^{-5}$, an extra higher harmonic (*m* > 2) of RMP results in a larger tearing mode response at the q = 2 rational surface. In particular, the amplitude of $b^r_{m/n=2/1}$ under the *m/n* = 2/1+4/1 RMP is the largest among all cases with higher harmonic superposition (*m* > 2), but still remains less than that of the *m/n* = 2/1 (× 2) RMP with $\delta\psi_{2,1}(\times2) = 4\times10^{-5}$. Consequently, the higher harmonics (*m* > 2) of the RMP could generate considerable driving effects at the q = 2 rational surface.

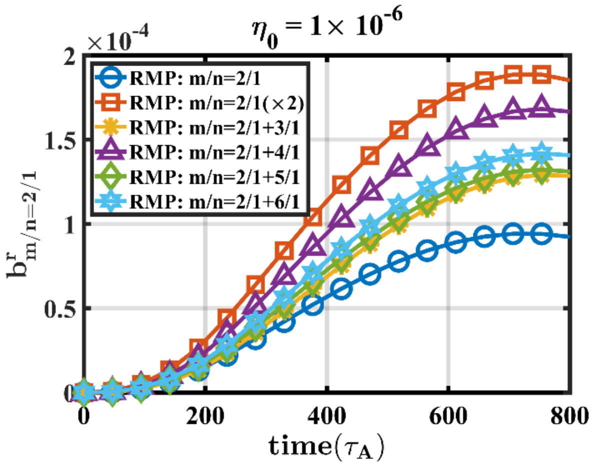

Figure 4. Time evolutions of $b^r_{m/n=2/1}$ with different harmonic compositions of RMP. The double-harmonic-RMP is combined with the *m*/*n* = 2/1 harmonic and an extra one with the same amplitude.

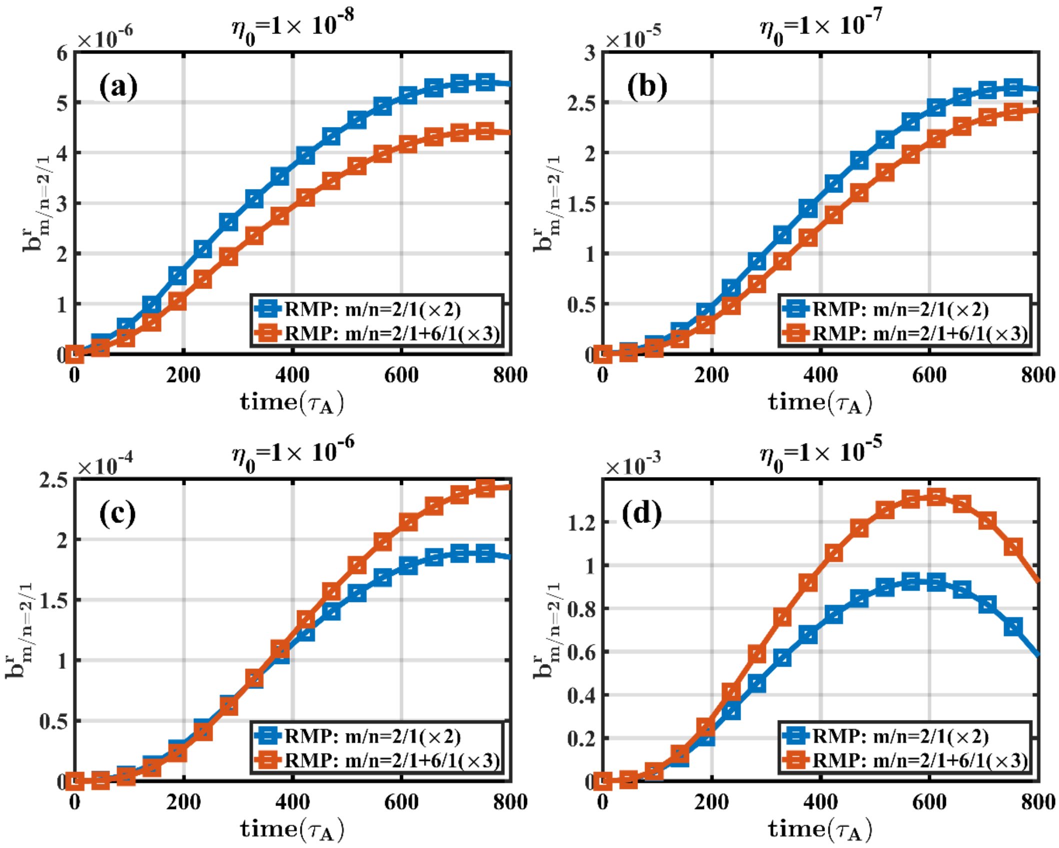

Figure 5. Time evolutions for amplitudes of $b^r_{m/n=2/1}$ with different harmonic compositions of RMP. The results from single-harmonic-RMP ($\delta\psi_{2,1} = 4\times10^{-5}$) are plotted using blue lines, while red lines represent results from the double-harmonic-RMP ($\delta\psi_{2,1} = 2\times10^{-5}$, $\delta\psi_{6,1} = 6\times10^{-5}$). The resistivities used in each simulation are (a) $\eta_0 = 10^{-8}$, (b) $\eta_0 = 10^{-7}$, (c) $\eta_0 = 10^{-6}$, and (d) $\eta_0 = 10^{-5}$, respectively.

In order to further understand how the higher harmonic to enhance the tearing mode response at the $q = 2$ rational surface, another comparison study is carried out by using different values of the resistivity based on two sets of RMP configuration with (a) $\delta\psi_{2,1} = 4\times10^{-5}$ (the single-harmonic-RMP), (b) $\delta\psi_{2,1} = 2\times10^{-5}$ and $\delta\psi_{6,1} = 6\times10^{-5}$ (the double-harmonic-RMP), respectively. A relatively large $m = 6$ component is applied to the double-harmonic-RMP to strengthen its driving effect. The time evolutions of $b^r_{m/n=2/1}$ at the $q = 2$ surface with different RMP configurations are plotted in Figure 5. When the resistivity is small, such as $\eta_0 = 10^{-8}$ shown in Figure 5 (a), the driving effect of the $m = 6$ harmonic at the $q = 2$ rational surface is relatively weak, resulting in the amplitude of $b^r_{m/n=2/1}$ becoming smaller in the double-harmonic-RMP compared to that in the single-harmonic-RMP. However, when the resistivity increases, the driving effect from the higher harmonic becomes more important. After the resistivity increases to $\eta_0 = 10^{-6}$ shown in Figure 5 (c), the amplitude of $b^r_{m/n=2/1}$ in the double-harmonic-RMP exceeds that of the single-harmonic-RMP.

Figure 6 exhibits the $b^r_{n=1}$ spectra corresponding to the cases in Figure 5 (a) and (c). For the low resistivity $\eta_0 = 10^{-8}$, as shown in Figure 6 (a) and (b), the penetration depth of $m = 2$ harmonic is limited outside the $q = 2$ rational surface for both types of RMPs. The $m = 6$ harmonic vanishes quickly before reaching the $q = 2$ surface. Consequently, the resultant $m = 2$ and $m = 6$ perturbations from the double-harmonic-RMP are almost independent of each other, and the $b^r_{m/n=2/1}$ is mainly driven by the $m = 2$ harmonic of the RMP. The spectrum is consistent with that shown in Figure 5 (a), where the amplitude of $b^r_{m/n=2/1}$ from the double-harmonic-RMP is lower than that of the single-harmonic-RMP. However, after the resistivity increases to $\eta_0 = 10^{-6}$, the penetration depths from both types of RMP are greatly boosted, which suggests that the large resistivity can largely reduce the current shielding and enhance the penetration of RMPs. Meanwhile, the results from the double-harmonic-RMP also become completely different. Due to the toroidal effect, the strong $m = 6$ harmonic in RMP generates a sequence of lower $b^r_{m,n}$ harmonics from $m = 5$ to $m = 2$ and propagates inward to the central plasma region. The longest arrow in Figure 6 (d) indicates the inward propagation direction of the RMP from the $m = 6$ harmonic to the $m = 2$ harmonic due to the toroidal effect. After successful penetration by the higher harmonic, the considerable $m = 3$ and $m = 4$ components are generated at the $q = 2$ rational surface, which could indirectly drive $b^r_{m/n=2/1}$. In addition, the $b^r_{m/n=2/1}$ component inside the $q = 2$ rational surface is also much larger than that of the single-harmonic-RMP. Therefore, for the double-harmonic-RMP, the inside and outside resonant driving (m = 2) and the non-resonant driving (m > 2) together result in the final amplitude of $b^r_{m/n=2/1}$ to exceed that of the single-harmonic-RMP, even though the direct m = 2 driving strength from the double-harmonic-RMP is only a half of the single-harmonic-RMP.

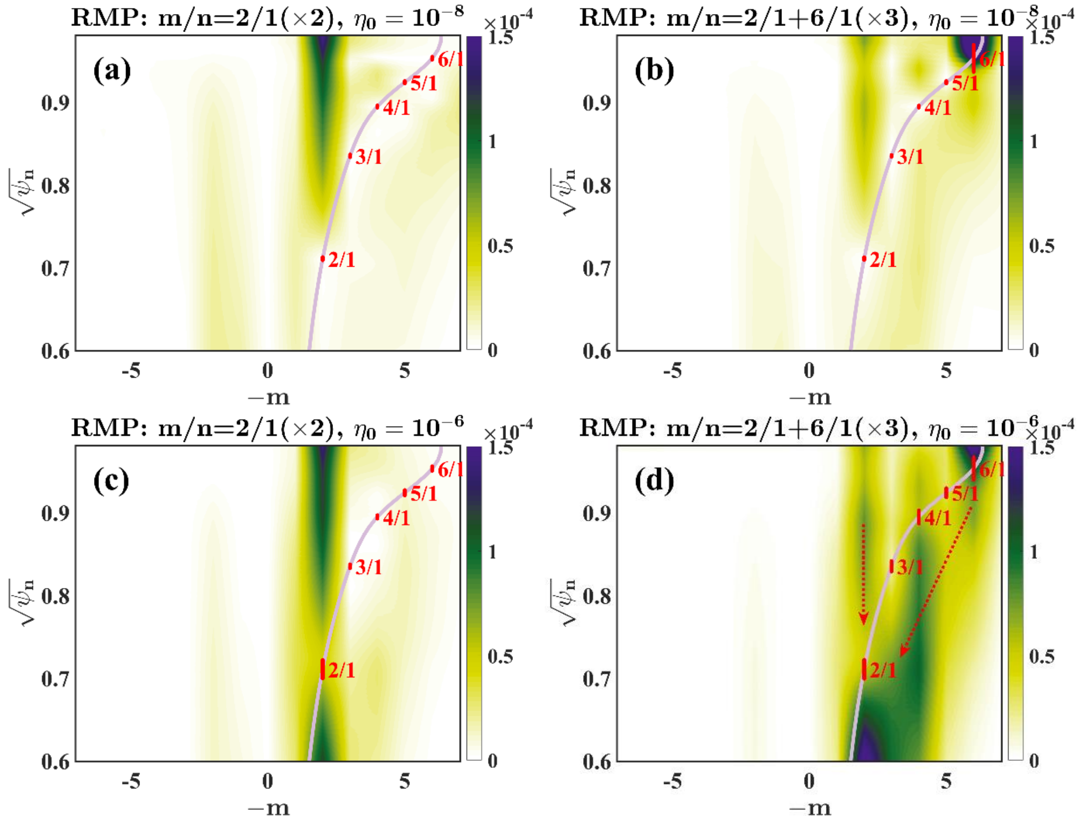

Figure 6. The radial distributions of the $b^r_{n=1}$ spectra at $t = 423\tau_A$ for (a) the single-harmonic-RMP ($\delta\psi_{2,1} = 4\times10^{-5}$, $\eta_0 = 10^{-8}$), (b) the double-harmonic-RMP ($\delta\psi_{2,1} = 2\times10^{-5}$, $\delta\psi_{6,1} = 6\times10^{-5}$, $\eta_0 = 10^{-8}$), (c) the single-harmonic-RMP ($\delta\psi_{2,1} = 4\times10^{-5}$, $\eta_0 = 10^{-6}$), and (d) the double-harmonic-RMP ($\delta\psi_{2,1} = 2\times10^{-5}$, $\delta\psi_{6,1} = 6\times10^{-5}$, $\eta_0 = 10^{-6}$).

The influences from the intrinsic kink and tearing instabilities (m/n = 1/1 resistive kink mode and m/n = 2/1 tearing mode) on the RMP penetration process is further examined by using artificially setting-up resistivity distribution. Two types of artificial resistivity distributions are shown in Figure 7. With the type-1 distribution, the small resistivity value ($\eta_0 = 10^{-8}$) is applied inside the q = 1 rational surface to reduce the growth rate of the m/n = 1/1 resistive kink mode, while the resistivity in the outer region (q > 1) remains at a high level ($\eta_0 = 10^{-6}$). It is found that, in comparison with the results of Figure 5 (c), the lower resistivity inside the q = 1 surface has a little effect on the evolution of $b^r_{m/n=2/1}$ at the q = 2 surface. As shown in Figure 8, the only difference resulted from the type-1 resistivity distribution is that $b^r_{m/n=1/1}$ at the q = 1 rational surface becomes much weaker because magnetic reconnection is suppressed due to the small resistivity. While the global mode structures of $b^r_{m/n}$ outside the q = 1 rational surface are almost identical between these two cases. Consequently, the fast growth of the m/n = 1/1 harmonic is the result of the external driving process rather than the intrinsic resistive kink instability.

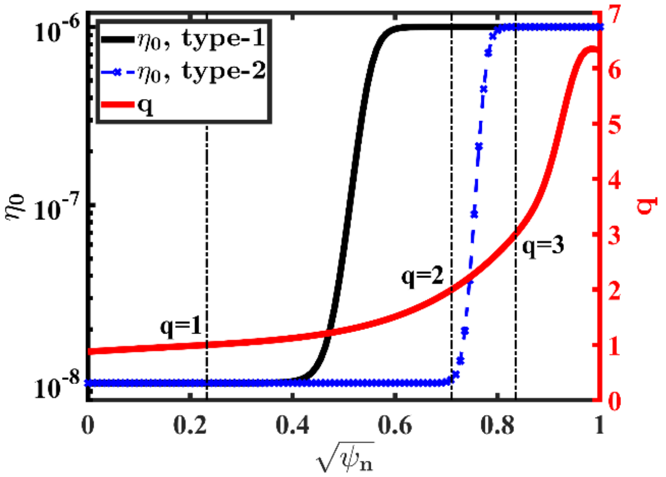

Figure 7. Profile of the safety factor (red line) reconstructed for discharge 52340 with the QSOLVER code and the two different types of the resistivity η_0 distributions: Type-1 (black line), the small resistivity value ($\eta_0 = 10^{-8}$) is applied inside the q = 1 rational surface, but the resistivity in the outer region (q > 1) remains at a high level ($\eta_0 = 10^{-6}$); Type-2 (blue line), the small resistivity value ($\eta_0 = 10^{-8}$) is applied inside the q = 2 rational surface, but the resistivity in the outer region (q > 2) keeps at a high level ($\eta_0 = 10^{-6}$).

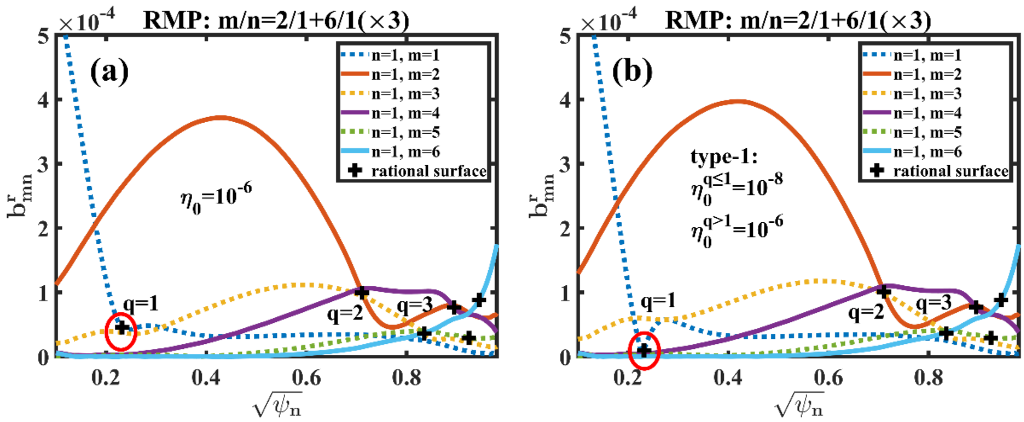

Figure 8. The radial structures of $b^r_{m,n}$ at $t = 800\tau_A$ with the double-harmonic-RMP for (a) the uniform η_0 resistivity distribution, $\eta_0 = 10^{-6}$, (b) the type-1 resistivity distribution with $\eta_0^{q\le1} = 10^{-8}$ and $\eta_0^{q>1} = 10^{-6}$.

With the type-2 resistivity distribution (the lower resistivity inside the q = 2 rational surface), the penetration properties of the single-harmonic-RMP and the double-harmonic-RMP become totally different. Firstly, due to the generation of the screen current, a strong shielding effect is observed in the mode structures of $b^r_{m/n=2/1}$ in Figure 9 (a) and δE_ϕ in Figure 10 (a). Thus, the single-harmonic-RMP penetration is blocked at the q = 2 rational surface, and the amplitude of the $b^r_{m/n=2/1}$ component inside the q = 2 surface is much weaker than that outside the surface. In contrast, with the double-harmonic-RMP applied as shown in Figure 9 (b), a series of intermediate non-resonant harmonics (m from 3~5) are greatly generated across the entire space. As a result, with the double-harmonic-RMP, the penetrated $b^r_{m/n=2/1}$ component inside the q = 2 surface is comparable with that outside the surface. With the indirect driving from non-resonant harmonics (m > 2) at the rational surface and the direct driving from resonant harmonic (m = 2) both inside and outside, the value of $b^r_{m/n=2/1}$ at the q = 2 surface far exceeds that of the single-harmonic-RMP, even though the external m = 2 driving strength in the single-harmonic-RMP case is doubled. Meanwhile, as shown in Figure 10 (b), the m/n = 1/1 perturbation resulted from the double-harmonic-RMP penetrates deeply into the central core region, and consequently, a strong kink mode is excited inside the q = 1 rational surface.

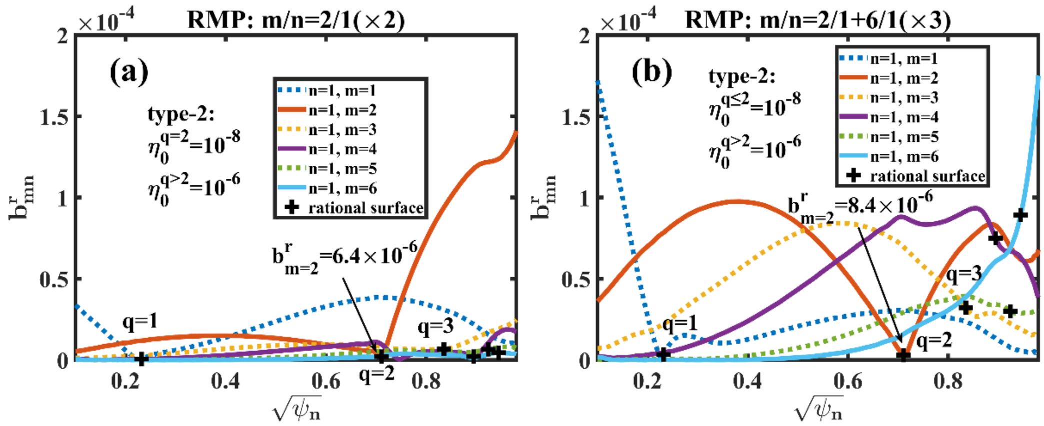

Figure 9. The radial structures of $b^r_{m,n}$ at $t = 800\tau_A$ with the type-2 resistivity distribution ($\eta_0^{q\le2} = 10^{-8}$ and $\eta_0^{q>2} = 10^{-6}$) for (a) the single-harmonic-RMP, (b) the double-harmonic-RMP.

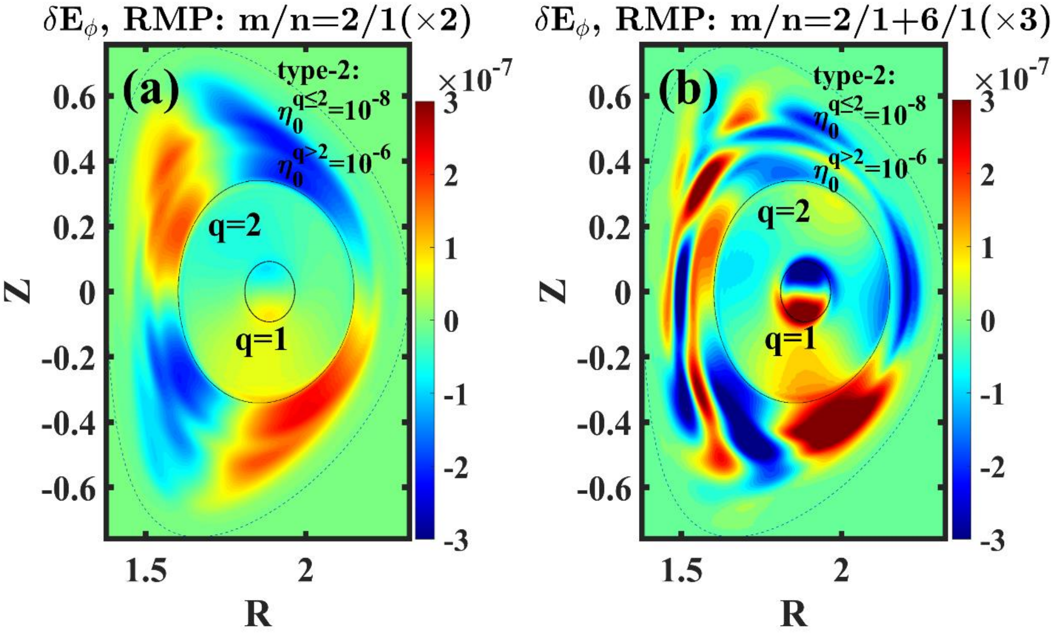

Figure 10. The mode structures of δE_ϕ at $t = 800\tau_A$ with the type-2 resistivity distribution, $\eta_0^{q\leq2} = 10^{-8}$ and $\eta_0^{q>2} = 10^{-6}$ for (a) the single-harmonic-RMP, and (b) the double-harmonic-RMP.

4.2 Poloidal harmonic filtering analysis and the multiple-harmonic-RMP

A supplementary study concerning the toroidal effect on RMP penetration was carried out using poloidal filtering analysis. The filtering analysis is applied in the linear EAST RMP simulation where the SOL has been retained and the vacuum RMP field is calculated based on the realistic RMP coils [18]. Because the Cartesian grids in the poloidal section are used in the CLTx code, poloidal filtering analysis demands two coordinate transformations with interpolations among Cartesian grids and magnetic flux grids inside the plasma boundary for carrying out the Fourier transformations while an asymptotic transition is applied between the plasma and SOL regions for numerical continuity. The original radial structure of $b_{m,n}^r$ under the $n = 1$ EAST RMP is plotted in Figure 11 (a). To analyze the numerical errors resulting from the interpolations from coordinate transformations, we conducted a controlling simulation by employing the interpolations and Fourier transformations while all harmonics are retained in the inverse Fourier transformation. The results shown in Figure 11 (b) indicate that the numerical errors due to these processes only lead to a limited decline of the $m = 2$ harmonic, but the errors' influences on higher harmonics ($m \geq 3$) are ignorable. After we removed the $m = 4$ component in the inverse Fourier transformation, the global amplitude of $m = 3$ is greatly reduced and its maximum value is almost only a half of its original level as shown in Figure 11 (c). Next, as shown in Figure 11 (d), after we removed more intermediate harmonics

(m = 4, 5, 6), the amplitude of the global m = 3 perturbation is further reduced. Another interesting phenomenon is that after removing the intermediate harmonics in the simulation, the amplitudes of the higher harmonics exhibit an enhancement, examples of which can be seen for the m = 5, 6 harmonics in Figure 11 (c), and the m = 7 harmonic in Figure 11 (d). By removing the intermediate harmonics, the inward propagation channel from higher harmonics to lower harmonics is stifled, this results in amplitude decline of the inside lower harmonics and flux accumulation at the outside higher harmonics.

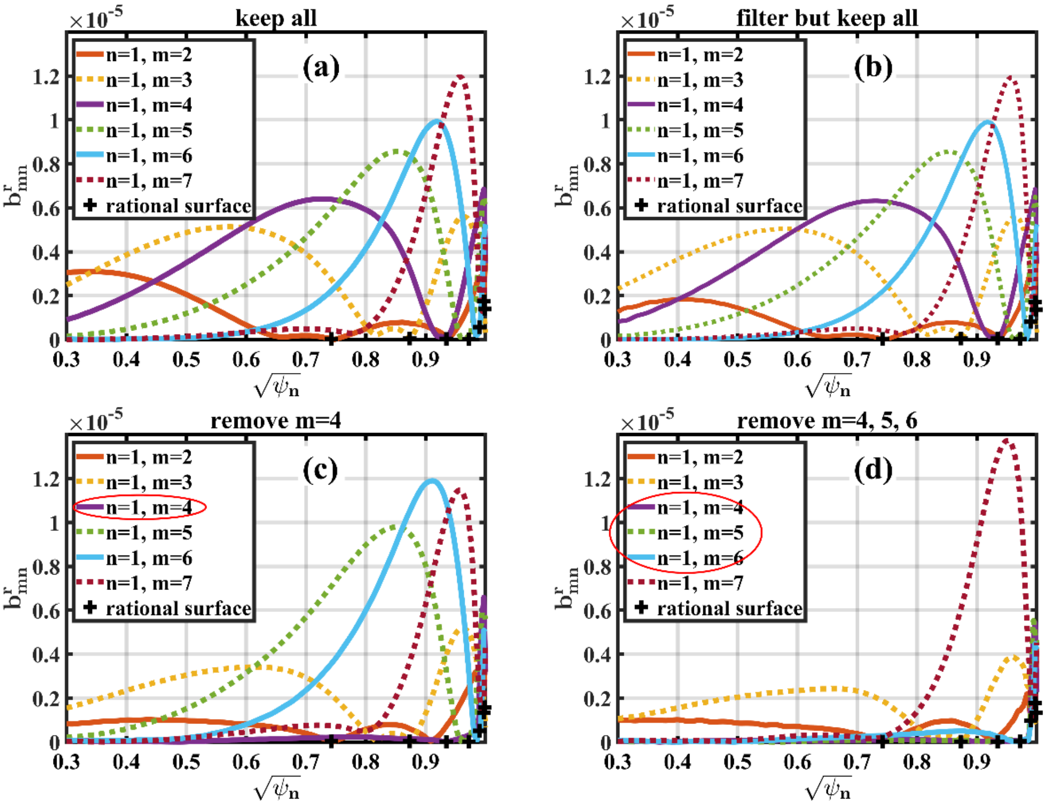

Figure 11. The radial structures of $b^r_{m,n}$ in the EAST $n = 1$ RMP simulation (a) without any specific treatment, (b) employing interpolations and Fourier transformations (all harmonics are retained), (c) artificially removing the m = 4 harmonic, and (d) artificially removing the m = 4, 5, 6 harmonics.

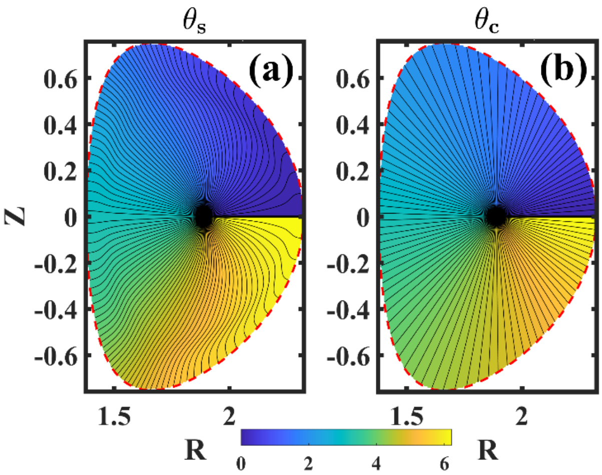

Figure 12. The distributions of the generalized poloidal angle θ_s of basic straight field line coordinate and the uniformly distributed poloidal angle θ_c.

Based on the above results about effects of the poloidal harmonics coupling, it is suggested that, in comparison with the single-harmonic-RMP, the multiple-harmonic-RMP could efficiently drive the development of MHD instabilities in the central plasma region. Therefore, a set of simulations is carried out to investigate roles of the multiple-harmonic-RMP on dynamic process of the tearing mode instabilities. The simulations are carried out with the equilibrium shown in Figure 7 and the RMPs are applied inside the plasma boundary with the formula of Eq. (7). The multiple-harmonic-RMP is implemented by changing the generalized poloidal angle θ_s of the basic straight field line coordinate in Eq. (7) into the uniformly distributed poloidal angle θ_c. Note that magnetic field lines are no longer straight in the $\theta_c - \phi$ plane. The distributions of θ_s and θ_c are shown in Figure 12 (a) and (b), respectively. The RMP with $\delta\psi_{2,1} = 4\times10^{-5}$ applied with the θ_s or θ_c dependency produced the radial distributions of the $b^r_{n=1}$ spectra as shown in Figure 13. The RMP depending on θ_s contains only the single m/n = 2/1 harmonic as shown in Figure 13 (a), while the latter one with the θ_c dependency contains multiple harmonics ranging from m = 2 ~ 7 as shown in Figure 13 (b). Apparently, the multiple-harmonic-RMP with the θ_c dependency creates the multiple harmonic perturbations at the pedestal region, which results in a large enhancement of the non-resonant components ($|m| > |nq|$) at the q = 2 rational surface due to the successful penetration of high harmonic perturbations. Consequently, the resulted tearing mode response at the q = 2 rational surface from the multiple-harmonic-RMP is much larger than that from the single-harmonic-RMP as shown by Figure 14.

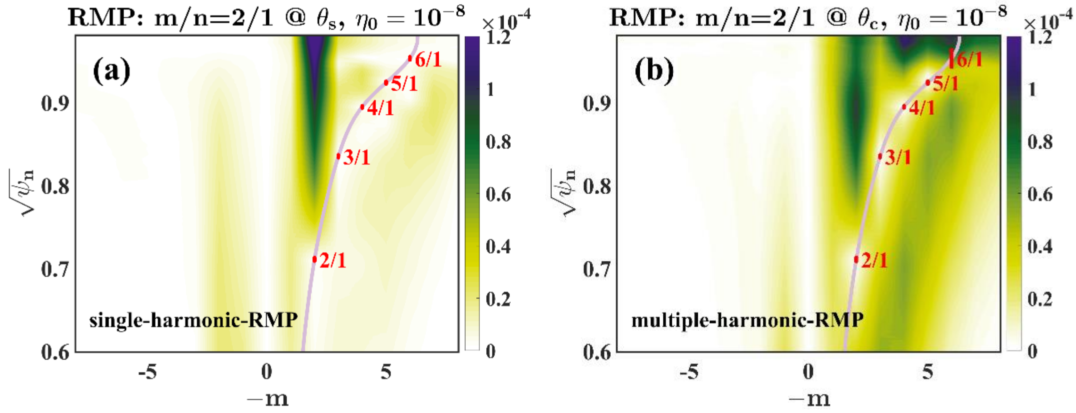

Figure 13. The radial distributions of the $b^r_{n=1}$ spectra at $t = 423\tau_A$ for (a) the single-harmonic-RMP and (b) the multiple-harmonic-RMP.

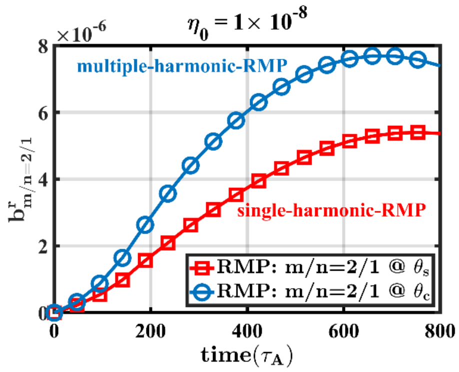

Figure 14. Time evolutions for amplitudes of $b^r_{m/n=2/1}$ with different RMPs: the red squares for the single-harmonic-RMP and the blue circles for the multiple-harmonic-RMP.

We also find from these present simulations that nonlinear effects on the inward penetration of higher harmonic RMPs are negligible due to the overlap condition $|\partial\zeta_r / \partial r| < 1$ being well satisfied. Concurrently, the linear simulations also give the same results as above. This indicates that the toroidal effect on RMP penetration is associated with the intrinsic symmetry breaking of the toroidal equilibrium magnetic field in the poloidal direction. Nevertheless, nonlinear effects may still be important when the magnetic islands grow large enough to affect the adjacent rational surfaces.

5 Conclusion and discussion

In the present paper, the CLTx code is used to study the $n = 1$ RMP penetration. The comparison study between linear and nonlinear modeling finds that with the presence of toroidal plasma rotation, the final steady state or saturated state for high resonant harmonics could be obtained in the initial value simulations of the CLTx code using the linearized MHD equations only. With this being the case, nonlinear effects are negligible since the magnetic islands evolve into a linearly saturated state due to plasma response and shielding. Therefore, the nonlinear simulations for discharge 52340 give the same results for rational surfaces around the pedestal as the linear results calculated by the MARS-F code [10, 20] and the linearized CLTx code [18]. However, without toroidal rotation, the linear MHD modeling performed by the CLTx code breaks down. This is because, without plasma rotation and nonlinear effects, the inside resonant harmonics in purely linear simulations give evolution dynamics with continuous growth where the final saturated state is not obtained unless the nonlinear terms are included. Consequently, this leads to the failure of predicting the shielding effect by plasma response. Therefore, for future Tokamaks with zero or low-speed toroidal rotation, such as ITER [39], the inclusion of nonlinear effects in the CLTx code will be necessary.

The simulations focusing on the toroidal effect in RMP penetration demonstrate that poloidal harmonics coupling [6, 30] is a consequence of the toroidal effect instead of nonlinear effects. With low resistivity, the single-harmonic-RMP is hard to penetrate the mode-rational surface because of the plasma screening effect, resulting in a truncation on the radial mode structure. On the other hand, the non-resonant components in the multiple-harmonic-RMP could avoid the plasma shielding, and thus play an effective role in the RMP penetration through the poloidal harmonics coupling. Consequently, with the inclusion of higher harmonics in RMP, the penetration by lower harmonics could become larger. The removal of the intermediate harmonics prevents the inward penetration of the outside higher harmonics, which results in an amplitude decrease (increase) of the inner lower (outer higher) harmonics. Finally, the observed mode coupling is mainly caused by the inhomogeneity of the toroidal equilibrium magnetic field rather than from nonlinear mode coupling. Consequently, nonlinear effects are unimportant for mode coupling when the toroidal effect dominates. This indicates a possible explanation for the similar results obtained by both the linear and nonlinear simulations.

Acknowledgments

This work was supported by the National Natural Science Foundation of China under Grant No. 11775188 and 11835010, the Special Project on High-performance Computing under the National Key R&D Program of China No. 2016YFB0200603, and the Fundamental Research Fund for Chinese Central Universities.

References

1. Zohm, H., *Edge localized modes (ELMs).* Plasma Physics and Controlled Fusion, 1996. **38**(2): p. 105-128.
2. Wagner, F., et al., *Regime of Improved Confinement and High-Beta in Neutral-Beam-Heated Divertor Discharges of the Asdex Tokamak.* Physical Review Letters, 1982. **49**(19): p. 1408-1412.
3. Boozer, A.H. and C. Nuhrenberg, *Perturbed plasma equilibria.* Physics of Plasmas, 2006. **13**(10): p. 102501.
4. Boozer, A.H., *Perturbation to the magnetic field strength.* Physics of Plasmas, 2006. **13**(4): p. 044501.
5. Nardon, E., et al., *Magnetohydrodynamics modelling of H-mode plasma response to external resonant magnetic perturbations.* Physics of Plasmas, 2007. **14**(9): p. 092501.
6. Orain, F., et al., *Non-linear modeling of the plasma response to RMPs in ASDEX Upgrade.* Nuclear Fusion, 2017. **57**(2): p. 022013.
7. Liu, F., et al., *Nonlinear MHD simulations of Quiescent H-mode plasmas in DIII-D.* Nuclear Fusion, 2015. **55**(11): p. 113002.
8. Becoulet, M., et al., *Mechanism of edge localized mode mitigation by resonant magnetic perturbations.* Phys Rev Lett, 2014. **113**(11): p. 115001.
9. Orain, F., et al., *Non-linear magnetohydrodynamic modeling of plasma response to resonant magnetic perturbations.* Physics of Plasmas, 2013. **20**(10): p. 102510.
10. Yang, X., et al., *Modelling of plasma response to 3D external magnetic field perturbations in EAST.* Plasma Physics and Controlled Fusion, 2016. **58**(11): p. 114006.
11. Li, L., et al., *Screening of external magnetic perturbation fields due to sheared plasma flow.* Nuclear Fusion, 2016. **56**(9): p. 092008.
12. Wade, M.R., et al., *Advances in the physics understanding of ELM suppression using resonant magnetic perturbations in DIII-D.* Nuclear Fusion, 2015. **55**(2): p. 023002.
13. Wingen, A., et al., *Connection between plasma response and resonant magnetic perturbation (RMP) edge localized mode (ELM) suppression in DIII-D.* Plasma Physics and Controlled Fusion, 2015. **57**(10): p. 104006.
14. Moyer, R.A., et al., *Validation of the model for ELM suppression with 3D magnetic fields using low torque ITER baseline scenario discharges in DIII-D.* Physics of Plasmas, 2017. **24**(10): p. 102501.
15. Izzo, V.A. and I. Joseph, *RMP enhanced transport and rotational screening in simulations of DIII-D plasmas.* Nuclear Fusion, 2008. **48**(11): p. 115004.
16. Pankin, A.Y., et al., *Modelling of ELM dynamics for DIII-D and ITER.* Plasma Physics and Controlled Fusion, 2007. **49**(7): p. S63-S75.
17. Becoulet, M., et al., *Screening of resonant magnetic perturbations by flows in tokamaks.* Nuclear Fusion, 2012. **52**(5): p. 054003.
18. Zhang, H.W., et al., *Penetration properties of resonant magnetic perturbation in EAST Tokamak.* Physics of Plasmas, 2019. **26**(11): p. 112502.
19. Xiao, W.W., et al., *Propagation Dynamics Associated with Resonant Magnetic Perturbation Fields in High-Confinement Mode Plasmas inside the KSTAR Tokamak.* Phys Rev Lett, 2017. **119**(20): p. 205001.
20. Sun, Y., et al., *Edge localized mode control using n= 1 resonant magnetic perturbation in*

the EAST tokamak. Nuclear Fusion, 2016. **57**(3): p. 036007.

21. Xiao, W.W., et al., *Location of the first plasma response to resonant magnetic perturbations in DIII-D H-mode plasmas.* Nuclear Fusion, 2016. **56**(6): p. 064001.
22. Lyons, B.C., et al., *Effect of rotation zero-crossing on single-fluid plasma response to three-dimensional magnetic perturbations.* Plasma Physics and Controlled Fusion, 2017. **59**(4): p. 044001.
23. Strauss, H.R., et al., *Extended MHD simulation of resonant magnetic perturbations.* Nuclear Fusion, 2009. **49**(5): p. 055025.
24. Ferraro, N.M., *Calculations of two-fluid linear response to non-axisymmetric fields in tokamaks.* Physics of Plasmas, 2012. **19**(5): p. 056105.
25. Reiser, D. and D. Chandra, *Plasma currents induced by resonant magnetic field perturbations in tokamaks.* Physics of Plasmas, 2009. **16**(4).
26. Kaveeva, E. and V. Rozhansky, *Screening of resonant magnetic perturbations taking into account a self-consistent electric field.* Nuclear Fusion, 2012. **52**(5).
27. Ferraro, N.M., et al., *Role of plasma response in displacements of the tokamak edge due to applied non-axisymmetric fields.* Nuclear Fusion, 2013. **53**(7): p. 073042.
28. Liu, Y.Q., et al., *ELM control with RMP: plasma response models and the role of edge peeling response.* Plasma Physics and Controlled Fusion, 2016. **58**(11): p. 114005.
29. Liu, Y.Q., et al., *Toroidal modelling of RMP response in ASDEX Upgrade: coil phase scan, q(95) dependence, and toroidal torques.* Nuclear Fusion, 2016. **56**(5): p. 056015.
30. Ryan, D.A., et al., *Toroidal modelling of resonant magnetic perturbations response in ASDEX-Upgrade: coupling between field pitch aligned response and kink amplification.* Plasma Physics and Controlled Fusion, 2015. **57**(9): p. 095008.
31. Zhang, H.W., et al., *Acceleration of three-dimensional Tokamak magnetohydrodynamical code with graphics processing unit and OpenACC heterogeneous parallel programming.* International Journal of Computational Fluid Dynamics, 2019. **33**(10): p. 393-406.
32. Zhang, W., Z.W. Ma, and S. Wang, *Hall effect on tearing mode instabilities in tokamak.* Physics of Plasmas, 2017. **24**(10): p. 102510.
33. Pustovitov, V.D., *Flux coordinates for tokamaks.* Plasma Physics Reports, 1998. **24**(6): p. 510-520.
34. Zheng, Z., et al., *Kinetic equilibrium reconstruction for the NBI- and ICRH-heated H-mode plasma on EAST tokamak.* Plasma Science & Technology, 2018. **20**(6).
35. Lao, L., et al., *Reconstruction of current profile parameters and plasma shapes in tokamaks.* Nuclear fusion, 1985. **25**(11): p. 1611.
36. Zhu, J., et al., *Nonlinear dynamics of toroidal Alfvén eigenmodes in the presence of tearing modes.* Nuclear Fusion, 2018. **58**(4): p. 046019.
37. Zhang, W., et al., *Core-crash sawtooth associated with m/n = 2/1 double tearing mode in Tokamak.* Plasma Physics and Controlled Fusion, 2019. **61**(7): p. 075002.
38. DeLucia, J., S.C. Jardin, and A.M.M. Todd, *An iterative metric method for solving the inverse tokamak equilibrium problem.* Journal of Computational Physics, 1980. **37**(2): p. 183-204.
39. Becoulet, M., et al., *Numerical study of the resonant magnetic perturbations for Type I edge localized modes control in ITER.* Nuclear Fusion, 2008. **48**(2): p. 024003.